Article

Dandelion-Like CuCo$_2$O$_4$@ NiMn LDH Core/Shell Nanoflowers for Excellent Battery-Type Supercapacitor

Wenhua Zhao [1,2], Xingliang Xu [1,*], Niandu Wu [2], Xiaodie Zhao [1] and Jiangfeng Gong [3,*]

1   Department of Applied Physics, Zhejiang University of Science and Technology, Hangzhou 310023, China
2   National Laboratory of Solid-State Microstructures, Collaborative Innovation Center of
    Advanced Microstructures, School of Physics, Nanjing University, Nanjing 210093, China
3   College of Science, Hohai University, Nanjing 211199, China
*   Correspondence: xlxu@zust.edu.cn (X.X.); jfgong@hhu.edu.cn (J.G.)

Abstract: Dandelion-like CuCo$_2$O$_4$ nanoflowers (CCO NFs) with ultrathin NiMn layered double hydroxide (LDH) shells were fabricated via a two-step hydrothermal method. The prepared CuCo$_2$O$_4$@NiMn LDH core/shell nanoflowers (CCO@NM LDH NFs) possessed a high specific surface area (~181 m^2·g^{-1}) with an average pore size of ~256 nm. Herein, the CCO@NM LDH NFs exhibited the typical battery-type electrode material with a specific capacity of 2156.53 F·g^{-1} at a current density of 1 A·g^{-1}. With the increase in current density, the rate capability retention was 68.3% at a current density of 10 A·g^{-1}. In particular, the 94.6% capacity of CCO@NM LDH NFs remains after 2500 cycles at 5 A·g^{-1}. An asymmetric supercapacitor (ASC) with CCO@NM LDH NFs//activated carbon (AC) demonstrates a remarkable capacitance of 303.11 F·g^{-1} at 1 A·g^{-1} with excellent cycling stability. The coupling and synergistic effects of multi-valence transition metals provide a convenient channel for the electrochemical process, which is beneficial to spread widely within the realm of electrochemical energy storage.

Keywords: CuCo$_2$O$_4$@NiMn LDH nanoflowers; core/shell; synergistic effect; battery-type; supercapacitors

1. Introduction

Supercapacitors have attracted extensive research attention due to the increasing demand for sustainable and reliable energy storage devices. Simultaneously, supercapacitors can bridge the gap between batteries and capacitors since they can provide power density and long cycle life [1,2]. Binary transition metal oxides have been considered to be promising candidates as electrodes for high-performance pseudo-capacitors due to their multiple redox reactions and high electrical conductivity [3–5]. Because of the various redox reactions and high conductivity, transition bimetallic oxides are regarded as the best candidates for high-performance pseudocapacitor electrode materials [6,7].

The electrode material with core/shell structures can provide more active sites to improve its conductivity, achieving unprecedented electrochemical performance. The main reason for this is that the core/shell structure can promote the rapid transfer of ions and electrons in the electrochemical process [8]. Moreover, the electrode material in the core possesses high conductivity, which can optimize the transmission path of charge. The shell with a higher surface area can further promote the mass transfer at the interface of the electrode and electrolyte, further providing more space for ion transport. In addition, more defects [9,10], such as oxygen vacancies, can be introduced using core/shell structures, which can alleviate the change in sample volume in the electrochemical test. In recent years, more and more efforts have been made to construct core/shell electrode materials, such as MnCo$_2$O$_4$@Ni(OH)$_2$ core-shell flowers [11], (Ni,Co)Se$_2$/NiCo-LDH core/shell [12], P-Ni(OH)$_2$@Co(OH)$_2$ core/shell [13], Mn(OH)$_2$-containing Co(OH)$_2$/Ni(OH)$_2$ core/shell [14], MoS$_2$@α-Fe$_2$O$_3$/CNTF [15], MnS@Ni(OH)$_2$

core/shell [16], Ni(OH)$_2$@NHCSs electrode [17], NiCoP@C@Ni(OH)$_2$ core/shell nanoarrays [18], and so on. The rational construction of the core/shell electrode greatly promotes the development of supercapacitors through a synergetic effect. Two-dimensional NiMn-layered hydroxide (NiMn LDH) with low cost demonstrates multiple valence states of transition metals, such as Ni and Mn, which can facilitate rich redox reactions in the electrochemical process [19,20]. At the same time, NiMn LDH increases the conductivity of electrode materials and accelerates ion transmission [21,22].

Herein, a CCO core is shelled with NiMn LDH, which forms CCO@NM LDH NFs' electrode material via two hydrothermal reactions. CCO@NM LDH NFs with core/shell structure can construct abundant oxygen vacancy defects to increase the large specific surface area of CCO@NM LDH NFs, which enables ions to freely insert and remove in the electrochemical process, thus improving the supercapacitor performance of composite electrode materials. As the anode material of supercapacitors, the discharge-specific capacitance of core/shell CCO@NM LDH NFs is as high as 2156.53 F·g^{-1} at a current density of 1 A·g^{-1}. Activated carbon and CCO@NM LDH NFs are used as the anode and cathode, respectively, for the construction of the asymmetric supercapacitor. The hybrid supercapacitor demonstrates a remarkable capacitance of 303.11 F·g^{-1} at 1 A·g^{-1}. It also provides a maximum energy density of 92.2 Wh·kg^{-1} at a power density of 730 W·kg^{-1}; moreover, and it shows excellent stability. Therefore, this work can be used as a guide for preparing new functional materials with high-performance supercapacitors.

2. Materials and Methods

2.1. Synthesis of Samples

The CCO@NM LDH is synthesized using a two-step hydrothermal reaction schematically shown in Scheme 1. Firstly, 4 mmol of Co(NO$_3$)$_2$·6H$_2$O and 2 mmol of Cu(NO$_3$)$_2$·6H$_2$O were dissolved in 80 mL of distilled water and ethanol with a volume ratio of 1:1 as the starting materials. A piece of Ni foam (NF, 2 × 4 cm^2) was submerged in the homogeneous solution and heated at 120 °C for 6 h using a hydrothermal reaction. Then, the CuCo precursor attached to NF surface was successfully obtained. the CuCo precursor powder was annealed at 350 °C for 6 h to obtain NF-loaded CuCo$_2$O$_4$. Secondly, Ni foam loaded with CuCo$_2$O$_4$ was used as a substrate for secondary hydrothermal growth in the following solution. The solution contains 0.713 g of NiCl$_2$·6H$_2$O and 0.198 g of MnCl$_2$·4H$_2$O, and 0.7 g of hexamethylenetetramine (HMT) and the NF-loaded CuCo$_2$O$_4$ were rinsed in 70 mL of distilled water. The reaction was conducted at 90 °C for 6 h. After the reaction, the mixture loaded on NF was washed and dried at 60 °C to obtain CCO@NM LDH NF samples.
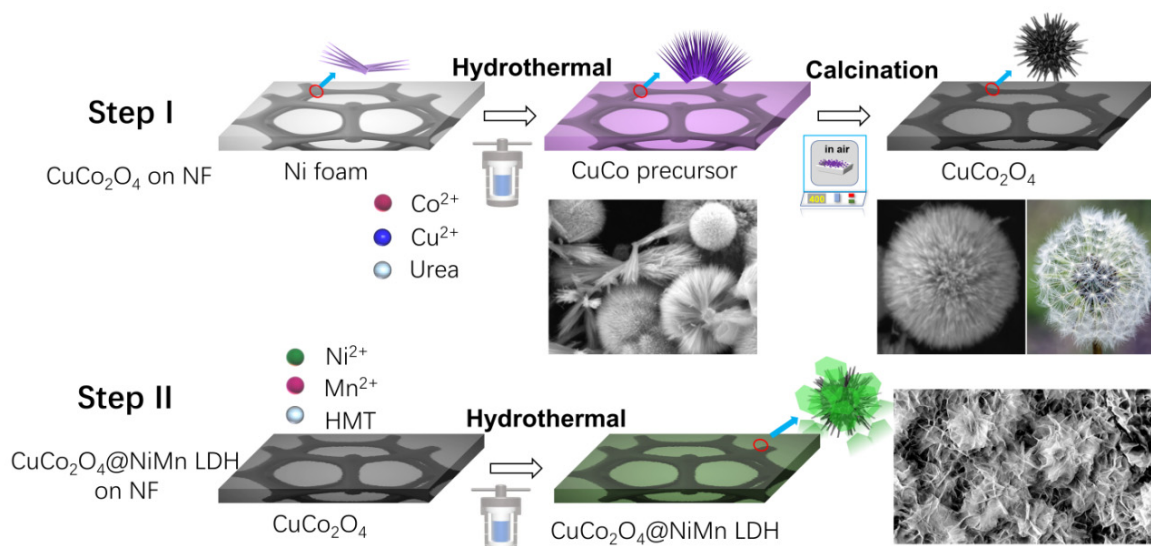
Scheme 1. Schematic illustration of the preparation process of CuCo$_2$O$_4$@NiMn LDH.

2.2. Characterization

A field emission scanning electron microscope (FE-SEM, s4800, Hitachi, Tokyo, Japan) and transmission electron microscope (TEM, JEM-1200EX, Tokyo, Japan) were used to characterize the morphology of the samples. Energy dispersive X-ray spectroscopy (EDS) was used to display the distribution of elements. X-ray diffractometer (XRD, td-3500, Heilongjiang, China) in Cu K target (α = 1.542 Å) was recorded at the 2θ scanning range of 10° to 80° Kα. The chemical states of elements were studied using X-ray photoelectron spectroscopy (XPS, model, uivac phi, Tokyo, Japan). The specific surface area was analyzed via BET JW-004 with nitrogen adsorption/desorption for 1 h.

3. Results and Discussions

To better investigate the influence on the morphology of the dandelion-like CCO@NM LDH NFs, a series of FE-SEM images were carried out to determine the evolution of the CuCo precursors. Scheme 1 shows that the morphologies of the CuCo precursor on Ni foam (NF) transformed from loosely assembled immature pine needle-like structures to densely stacked dandelion-like spheres after high-temperature annealing. Subsequently, ultrathin NiMn LDH layers were hydrothermally grown on the surface of dandelion-like $CuCo_2O_4$ nanoflowers, as illustrated in Figure 1a, which greatly increased the specific surface area of the CCO-NM LDH NFs, subsequently providing more active sites. The FE-SEM images of the $CuCo_2O_4$ sample and $CuCo_2O_4$-NiMn LDH sample are shown in Figure S1a,b and Figure S1c,d, respectively (see Supplementary Materials). Dandelion-like CCO NFs are evenly dispersed on the surface of the NF with a size of about 1 μm. As shown in Figure 1b, dandelion-like CCO NFs are shelled with ultrathin NiMn LDH. The nanoflowers are interwoven, and their size increases to about 2 μm. The elemental distribution on CCO and CCO@NM LDH NFs was further investigated by performing energy dispersive (EDS) and elemental mapping in Figure S2 and Figure 1c–i, respectively. Cu, Co, Ni, Mn, and O are homogeneously distributed on the entire surface of the CCO@NM LDH NFs, confirming the successful synthesis of a heterostructure in which NiMn LDH has grown on the surface of the CCO NFs.

The morphology and crystallinity of $CuCo_2O_4$-NiMn LDH material were further analyzed using high-resolution transmission electron microscopy (HRTEM) and XRD measurements. As shown in Figure 2a, the CCO@NM LDH material appears as a high-light transmission, indicating that the sample is also ultrathin with good dispersion and no obvious stacking. The size of the CCO@NM LDH material is as large as that shown in the SEM analysis. Notably, the clear and orderly lattice spacing of CCO-NM LDH NFs is 0.248 nm in Figure 2b which is, consistent with the (009) plane of NiMn LDH. From Figure 2c, two obvious diffraction rings of the selected area electron diffraction (SAED) also correspond to (003) and (009) planes of CCO@NM LDH material. The phase purity and crystal structure of the CCO and CCO@NM LDH NFs were investigated using XRD in Figure 2d. Several peaks are observed at 2θ values of 18.88, 31.08, 36.62, 38.30, 44.52, 58.96, and 64.79°, which are indexed to the (111), (220), (311), (222), (400), (511), and (440) crystal planes of cubic $CuCo_2O_4$ (JCPDS No. 78-2177). Then, the diffraction peaks of LDH can be reasonably indexed to a series of crystal planes, such as (003), (006), (009), and (110). This demonstrates the successful preparation of spinel $CuCo_2O_4$ shelled with NiMn LDH. No peaks of impurities such as copper oxides and cobalt oxides were found, confirming the high purity of the product. The synergistic effect of dandelion-like $CuCo_2O_4$ and ultrathin NiMn LDH resulted in the successful preparation of CCO@NM LDH NFs with good crystallinity.
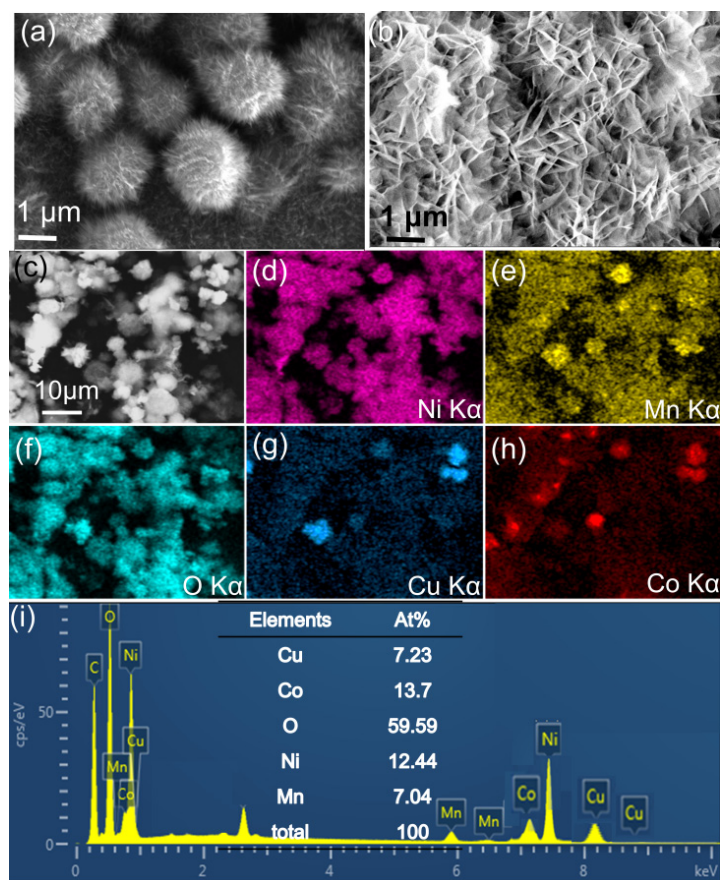
Figure 1. FE-SEM of (**a**) CuCo$_2$O$_4$ sample and (**b**) CuCo$_2$O$_4$@NiMn LDH sample. (**c–i**) EDS and mapping of CuCo$_2$O$_4$@NiMn LDH sample.
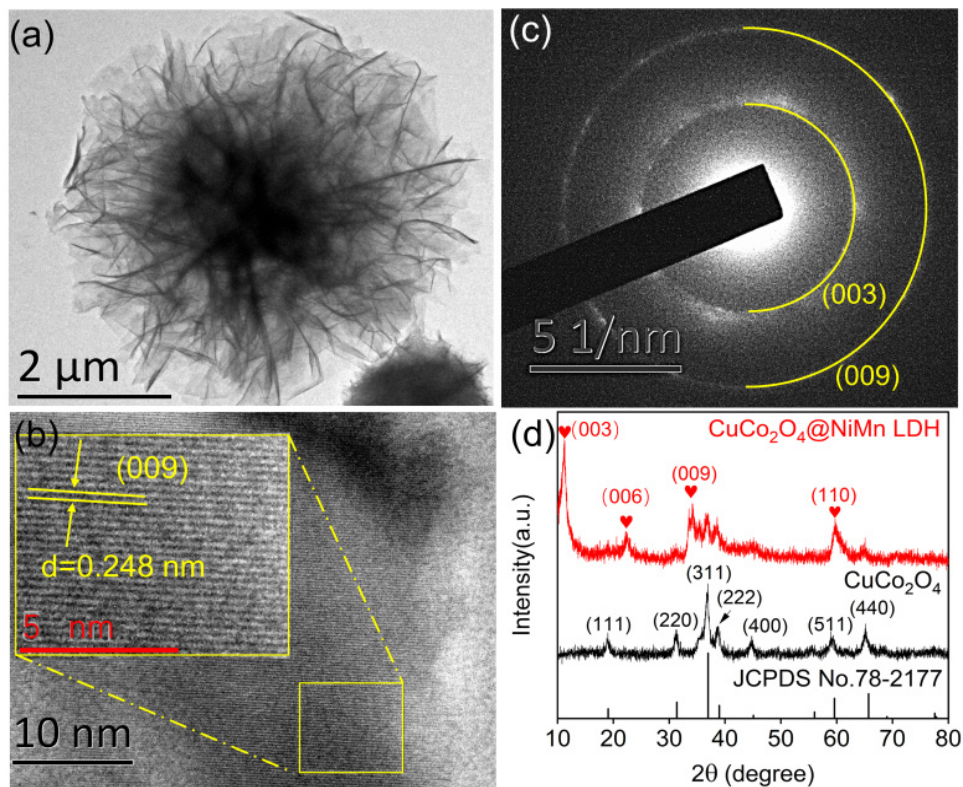
Figure 2. (**a**) TEM, (**b**) HRTEM, (**c**) SAED, and (**d**) XRD pattern of CuCo$_2$O$_4$-NiMn LDH sample.

As shown in Figure 3, XPS is used to identify the chemical state. The full XPS spectrum of CCO and CCO@NM LDH NFs is illustrated in Figure 3a. There is no interference from other impurity elements in the prepared samples. Figure 3b–d demonstrates XPS high-resolution spectra for Cu 2p, Co 2p, and O 1s, respectively. There are two sharp peaks at 952.6 eV and 932.6 eV, corresponding to Cu $2p_{3/2}$ and Cu $2p_{1/2}$, respectively [23]. The Co 2p spectrum in Figure 3c can be deconvoluted into peaks at 778.4 eV and 793.3 eV, in agreement with Co^{3+}, while peaks at 780.1 eV and 794.8 eV can be corresponded to Co^{2+}. Moreover, Co^{2+} and Co^{3+} co-exist in the $CuCo_2O_4$ sample and CCO@NM LDH NFs. It should be noted that the peak at 528.45 eV in the O1s spectrum disappears in the obtained CCO@NM LDH compared with $CuCo_2O_4$. The peak in the O1s spectrum of $CuCo_2O_4$ is fitted into three subpeaks, corresponding to O_L (528.4 eV), O_{OH} (529.9 eV), and O_V (531.1 eV). The O_L peak is ascribed to the Cu−O and Co−O bonds in Figure 3d. The O_{OH} peak is indexed to the −OH group [24]. O_L almost disappears with the synergistic effect of the core/shell structure. The appearance of O_W, located at 532.4 eV, induced physically and chemically absorbed water molecules on the surface of CCO@NM LDH NFs [25]. Obviously, O_V increases due to the transformation of O_L, and O_V represents oxygen vacancy. Meanwhile, peaks at 855.6 eV and 873.2 eV correspond to Ni $2p_{3/2}$ and Ni $2p_{1/2}$ in the Ni 2p spectrum in Figure 3e, respectively. This indicates that Ni exists in a +2 valence state [26]. Similarly, there is a peak at 652.27 eV in the Mn $2p_{1/2}$. The peak of Mn $2p_{3/2}$ at 641.80 eV is divided into two peaks, which demonstrates that Mn is present in the compound, similar to Mn^{3+} in Figure 3f [27].
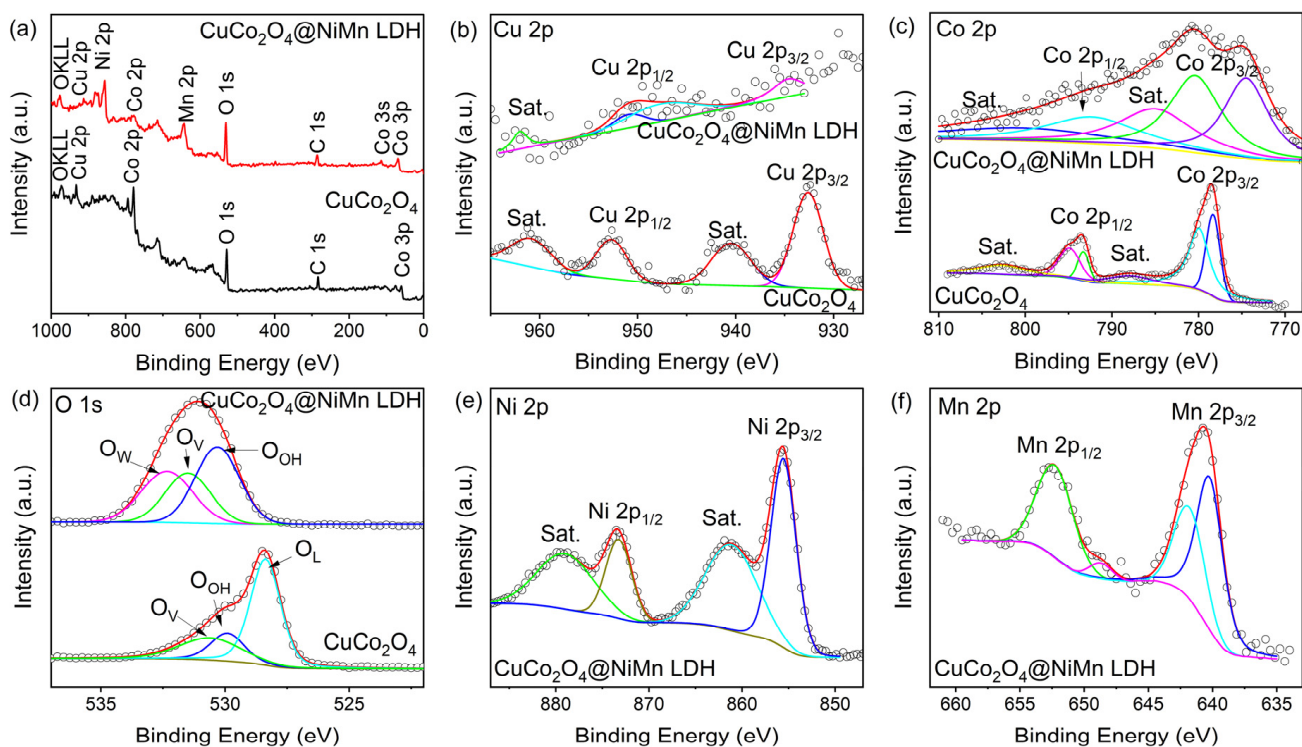

Figure 3. (**a**) XPS full spectrum. High-resolution XPS images of (**b**) Cu 2p, (**c**) Co 2p, (**d**) O 1s, (**e**) Ni 2p, and (**f**) Mn 2p of $CuCo_2O_4$ sample and $CuCo_2O_4$@NiMn LDH samples.

It can be speculated that an increase in oxygen vacancy provides more active sites for electrochemical processes. At the same time, the BET-specific surface area of the CCO@NM LDH NFs is more likely to be characterized as in Figure 4. Accordingly, the specific surface area of the CCO@NM LDH NFs (~181 $m^2 \cdot g^{-1}$) is 3.2 times that of the CCO NFs (~56.5 $m^2 \cdot g^{-1}$) in Figure 4a,b. The BJH desorption average pore diameter of CCO@NM LDH NFs is estimated to be 256 nm, which is much larger than bare CCO NFs. These results indicate that CCO@NM LDH NFs possess a larger surface and abundant macropores. The

large and specific surface area with a core/shell structure can offer abundant active sites for electrochemical reactions, which is convenient for the addition of more channels in the process of ion transport.
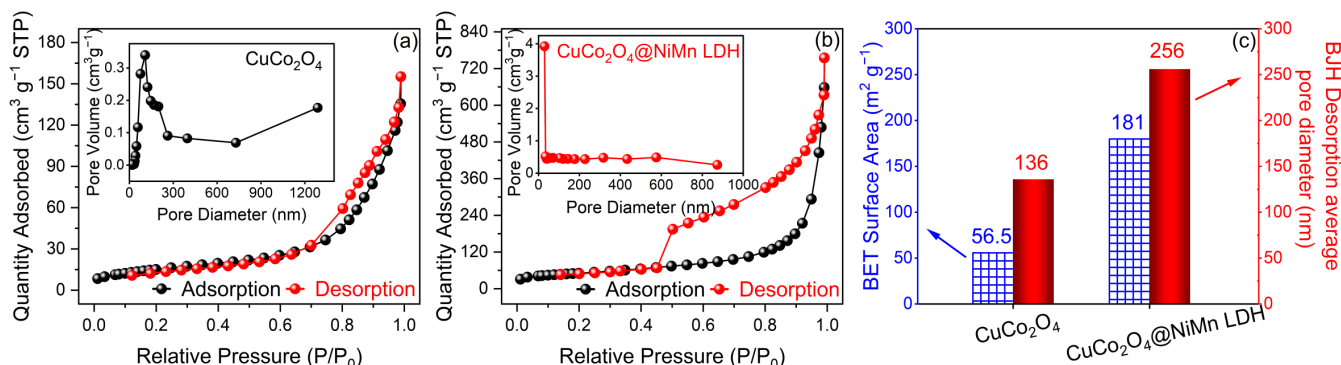

Figure 4. BET plots and BJH plots of (**a**) $CuCo_2O_4$ and (**b**) $CuCo_2O_4$@NiMn LDH. (**c**) BET surface area and pore diameter of $CuCo_2O_4$ and $CuCo_2O_4$@NiMn LDH samples.

Due to its abundant oxygen vacancy defects and highly specific surface area, the CCO@NM LDH NFs were speculated as a high-performance electrode material for supercapacitors. The capacitive properties of the as-obtained CCO NF, NiMn LDH, and CCO-NM LDH NF electrodes are measured using CV, GCD, and EIS tests. Figure 5a manifests the CV plots of the CCO NF, NiMn LDH, and CCO@NM LDH NF electrodes in a potential of 0–0.8 V at a scanning rate of 10 mV·s^{-1}. It is noted that the CCO@NM LDH NF electrodes show a better capacity than that of the CCO NFs and NiMn LDH electrodes. Similarly, the GCD plots of all samples at 1 A·g^{-1} are illustrated in Figure 5b. With the increase in scanning rate, the oxidation peaks in the CV curves of CCO@NM LDH NFs move to the direction of high voltage, whereas the reduction peaks move to the direction of low voltage, as shown in Figure 5c. Figure S5 demonstrates the specific capacitance values of the CCO@NM LDH electrode at different scan speeds [28]. These results are attributed to the internal resistance of the electrode [29]. From the GCD curves in Figure 5d, the specific capacitance values of the CCO@NM LDH electrode at current densities of 1 A·g^{-1}, 2 A·g^{-1}, 4 A·g^{-1}, 5 A·g^{-1}, 6 A·g^{-1}, 8A·g^{-1}, 10 A·g^{-1}, and 20 A·g^{-1} are 2156.53 F·g^{-1}, 2003.85 F·g^{-1}, 1826.88 F·g^{-1}, 1756.58 F·g^{-1}, 1692.79 F·g^{-1}, 1591.68 F·g^{-1}, 1472.79 F·g^{-1}, and 882.97 F·g^{-1}. Meanwhile, the obvious voltage platform at different current densities indicates that the CCO@NM LDH electrode is made of a battery-type capacitor. The GCD curves of each electrode show excellent reversible redox behavior and pseudo-capacitance characteristics, which is consistent with the corresponding redox reaction in CV. With an increase in current density, the rate capability retention is 68.3% at a current density of 10 A·g^{-1}. For comparison, CV and GCD plots of CCO NFs and NiMn LDH electrodes are given in Figure S3. We can see from Figure 5e that the discharge capacitance of the CCO@NM LDH NFs is 2156.53 F·g^{-1} at a current density of 1 A·g^{-1}, which is far higher than that of the CCO (~164.51 F·g^{-1}) and NiMn LDH samples (~1129.29 F·g^{-1}). This is because CCO@NM LDH NFs with a large and specific surface area make better contact with the electrolyte as an active substance. The Nyquist plots of the CCO NF, NiMn LDH, and CCO@NM LDH NF electrodes are shown in Figure 5f. Meanwhile, the corresponding equivalent circuit diagram is shown in Figure S6, which consists of four major components, namely, solution resistance (R$_S$), charge transfer resistance (R$_{CT}$), double layer capacitive (C$_{dl}$), and Warburg impedance (Zw) [30,31]. It is found that the CCO@NM LDH NF electrode possesses the smallest diffusion and charge transfer resistance, suggesting that the CCO@NM LDH NF electrode has good electronic conductivity and fast ion diffusion behaviors. After 5000 cycles, the capacity of CCO@NM LDH NFs at 5 A·g^{-1} is still 94.6%, which demonstrates the outstanding cycle stability.

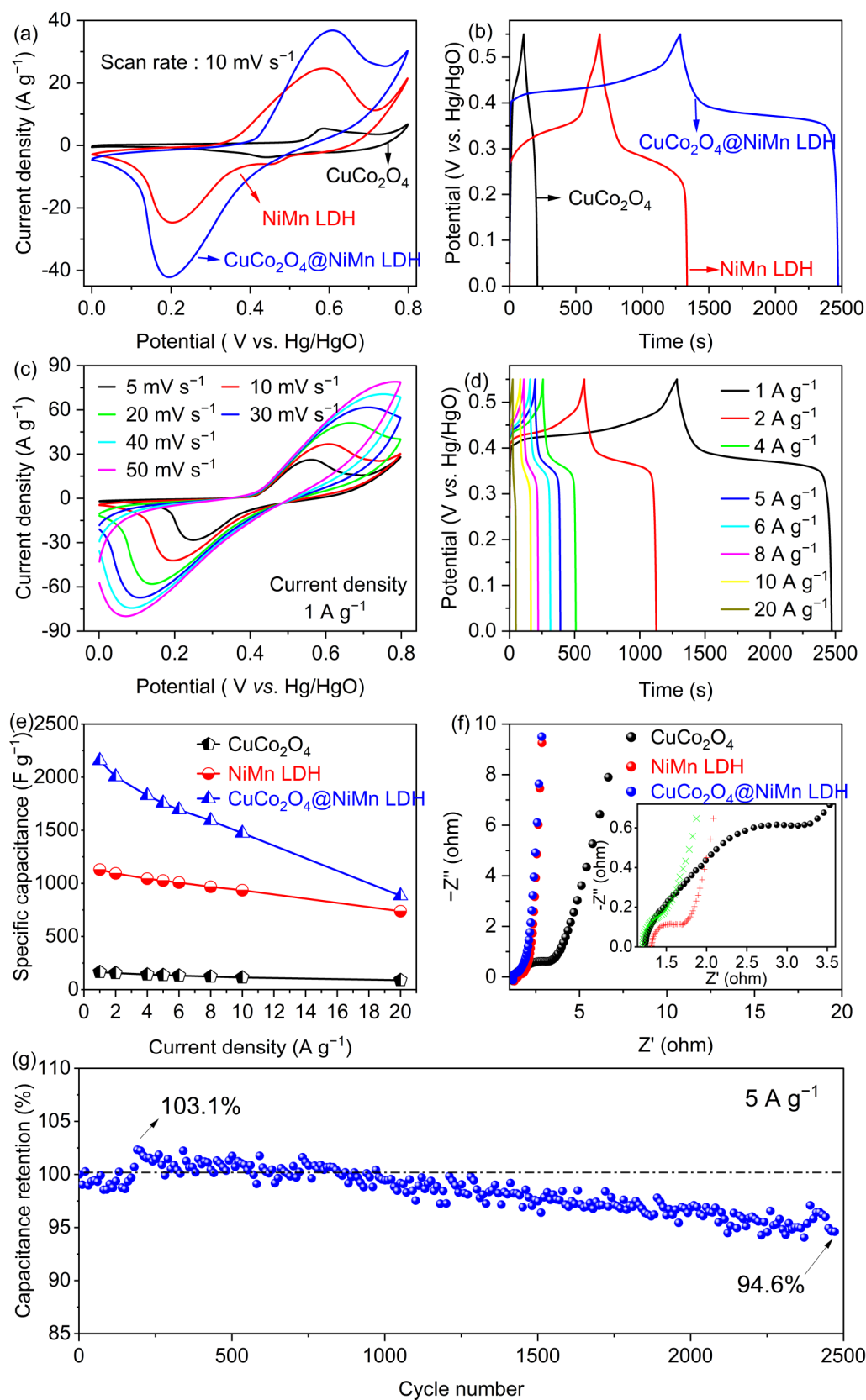**Figure 5.** (**a**) CV and (**b**) GCD plots of all samples at 10 mV·s^{-1} and 1 A·g^{-1}, respectively. (**c**) CV plots of CuCo$_2$O$_4$@NiMn LDH at different scan rates, (**d**) GCD plots of CuCo$_2$O$_4$@NiMn LDH at different current densities, (**e**) variation of specific capacitance with current density for all samples, (**f**) EIS diagram and (**g**) cyclic stability of CuCo$_2$O$_4$@NiMn LDH sample.

The storage methods of electrode charges are divided into surface capacitance control and diffusion control [32]. The process of energy storage depends on the relationship between peak current density and the power of sweep speed: $i = av^b$. The CV curves of the CCO@NM LDH NF electrodes at a low scanning speed were tested to thoroughly understand the mechanism of charge storage inhibition in the system in Figure 6c and Figure S4, so as to ensure that ions and electrons could fully participate in the reaction. i_a represents the peak current density of the oxidation peak in the oxidation process, and v is the scanning rate. When b is close to 0.5, the electrochemical process mainly depends on Faradic intercalation limited by diffusion; when $0.5 < b < 1$, the behavior is generally defined by the capacitance of the material in the electrode. Notably, the b value of the CCO@NM LDH NFs is the largest (0.748), reflecting that it has faster reaction kinetics in Figure 6a. Accordingly, the charge transfer process of the NiMn LDH sample is mainly controlled by diffusion, which indicates that the CCO@NM LDH NFs display battery-type behavior. In contrast, the b value of the $CuCo_2O_4$ sample as the core is 0.647. With an increase in scanning speed, the contribution of CCO@NM LDH NFs is almost entirely shown by capacitance in Figure 6d, which indicates that the charge storage controlled by the surface capacitance is dominant.
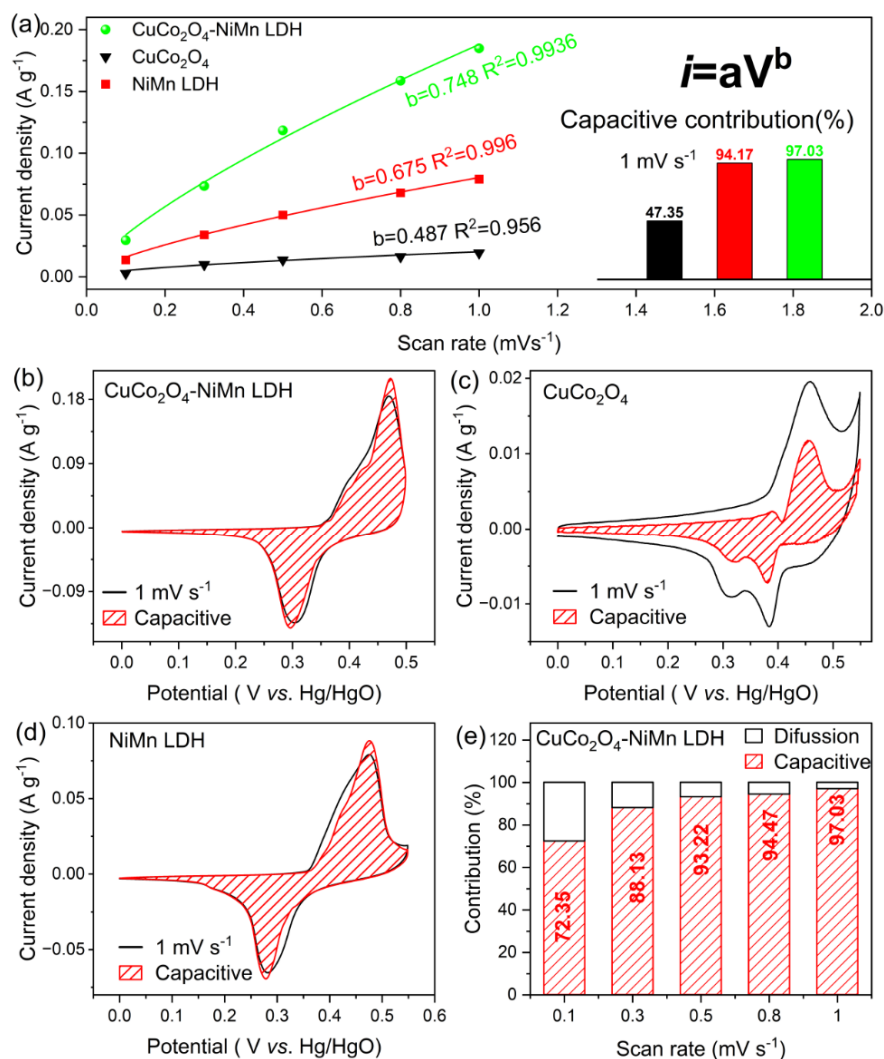

Figure 6. (**a**) b values of all samples at their respective oxidation peak positions. (**b**,**c**) Cyclic voltammetry profiles were collected at a scan rate of 1 mV·s^{-1} for the (**b**) CuCo$_2$O$_4$@NiMn LDH sample, (**c**) CuCo$_2$O$_4$ sample, and (**d**) NiMn LDH sample. The capacitive- and diffusion-controlled contribution to the current response represented by pink and white areas. (**e**) Capacitive- and diffusion-controlled contributions at different scan rates of all samples.

In view of its excellent capacitance performance as three electrodes, CCO@NM LDH NF, as the positive electrode, is assembled into an asymmetric capacitor. Meanwhile, activated carbon (AC) is the negative electrode, as shown in Figure 7a. The potential windows in Figure 7b of AC and CCO@NM LDH NFs come from $-0.7–0$ V and $0–0.8$ V, respectively. Figure 7c shows the CV curves of CCO@NM LDH//AC in different voltage windows (1.2–1.8 V) at a scanning speed of 30 mV·s^{-1}. When the potential window increases from 1.2 V to 1.5 V, the shape of the CV curve basically remains stable. We further confirm the rationality of the potential window through the GCD curve illustrated in Figure 7d. By synthesizing the GCD and CV curves, it is feasible to select the 0–1.5 V potential window for the assembled capacitor, i.e., CCO@NM LDH//AC. The combination of the electric double-layer capacitance and the pseudocapacitance of the storage device can be reflected by the obvious redox peak in the CV curve and the obvious potential platform in the GCD diagram [33,34]. Firstly, the CV curves (Figure 7d) of the asymmetric capacitor CCO@NM LDH//AC in the voltage window of 0–1.5 V were tested at different sweeping speeds, which displays that the asymmetric capacitor can effectively transport electrons. According to the GCD curve (Figure 7f), the discharge-specific capacitance of the asymmetric capacitor is 303.11 F·g^{-1} at a current density of 1 A·g^{-1}. When the current density increases to 20 A·g^{-1}, the specific capacitance of CCO@NM LDH//AC is still as high as 128 F·g^{-1}, as shown in Figure 7i. With the change in current density, the coulombic efficiency is maintained at around 100%. The assembled asymmetric capacitor device provides the maximum energy density of 92.2 Wh·kg^{-1} at a power density of 730 W·kg^{-1}. At the same time, the energy density is maintained at 39.55 Wh·kg^{-1} under the power density of 14,831 W·kg^{-1}. This suggests that CCO@NM LDH NFs with a core-shell structure demonstrate a large specific surface area, thus providing more active sites for the electrochemical process. According to the XPS results, the NiMn LDH shell also increases abundant oxygen vacancies in CCO@NM LDH NFs, which means that more free ions and electrons can be oxidized and reduced conveniently to improve the supercapacitor's performance. In addition, the device shows excellent stability in that its specific capacitance is 85.28% compared with that after 5000 cycles. Because of the advantages of traditional batteries and capacitors, supercapacitors not only share the high-energy density of batteries, but also express the high-power density of capacitors. In summary, the battery-type supercapacitor composed of CCO@NM LDH NFs is a promising energy storage device.
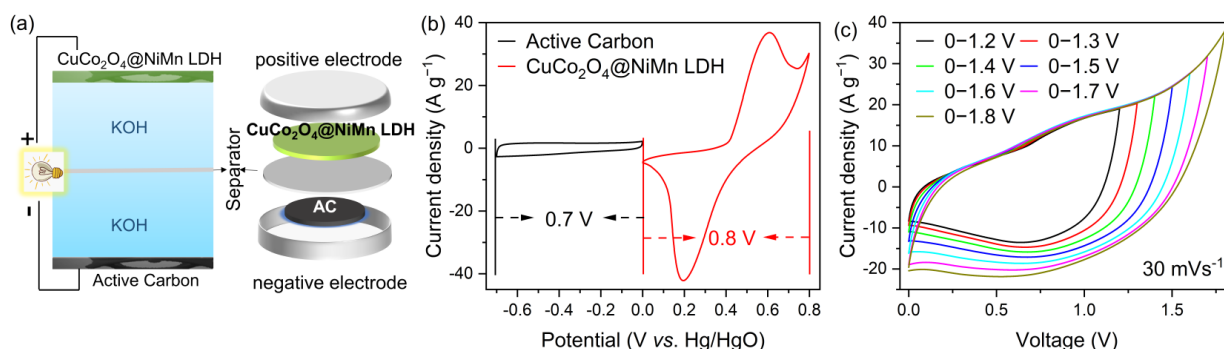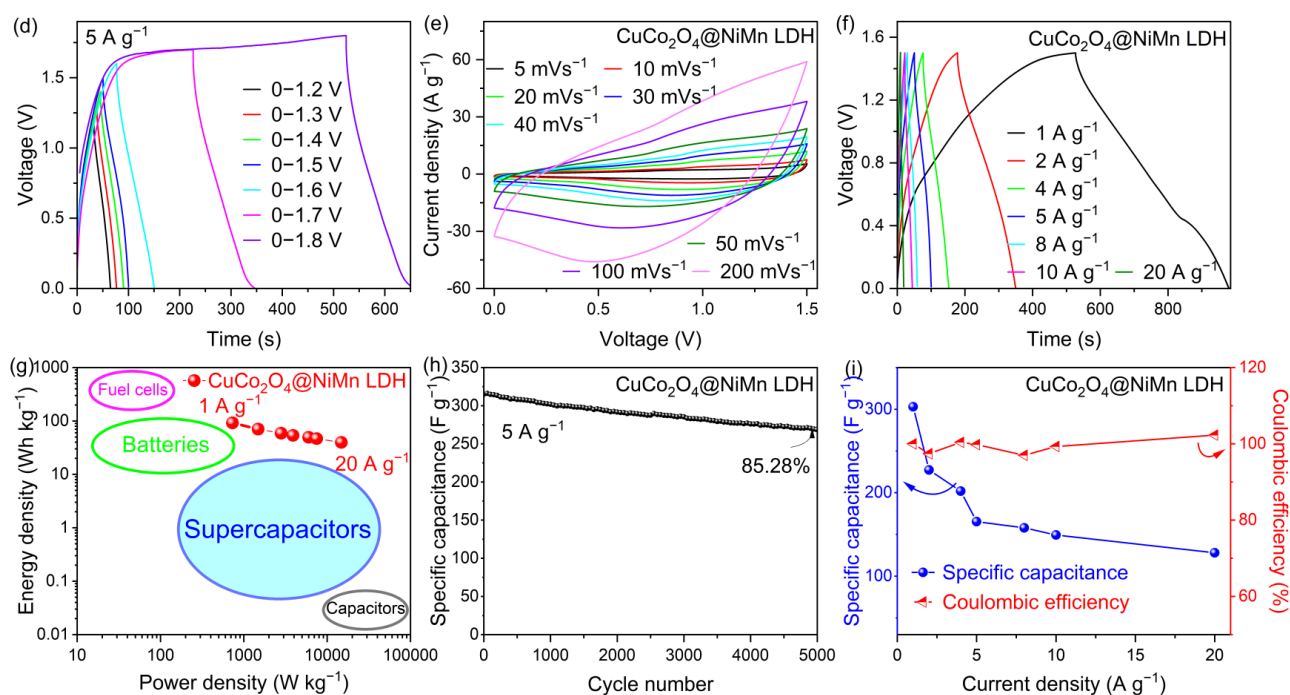

Figure 7. *Cont*.

Figure 7. Electrochemical properties of (**a**) the assembled button-type CuCo$_2$O$_4$@NiMn LDH//AC asymmetric capacitors. (**b**) CV profiles of CuCo$_2$O$_4$@NiMn LDH/NF and AC/NF electrodes at 50 mV·s^{-1}. (**c**) CV curves of different voltage windows, (**d**) GCD curves for different voltage windows, (**e**) CV curves of different scan rates in the range of 0–1.5 V, (**f**) GCD curves at different current densities in the range of 0–1.5 V, (**g**) Ragone correlation between energy density and power density, (**h**) cyclic stability, (**i**) capability and Coulomb efficiency at different current densities.

4. Conclusions

Dandelion-like CCO@NM LDH NFs with core/shell structure were synthesized via a two-step hydrothermal method. NiMn LDH was used as the shell to form the large and specific surface area of the CCO@NM LDH NFs (~181 m^2·g^{-1}) with more oxygen vacancy defects. Notably, the structures can provide a strong guarantee for the ions and electrons to enter and de-intercalate conveniently in the electrochemical process. As the anode material of supercapacitor, the discharge-specific capacitance is as high as 2156.53 F·g^{-1} at a current density of 1 A·g^{-1}. Meanwhile, CCO@NM LDH NF electrodes also show excellent stability. When AC and CCO@NM LDH are used as the anode and cathode of the asymmetric hybrid capacitor, respectively, the device can provide a maximum energy density of 92.2 Wh·kg^{-1} at a power density of 730 W·kg^{-1}. With impressive electrochemical performances, CCO@NM LDH NFs act as a battery-type electrode material on high-performance supercapacitors for energy storage.

References

1. Guan, X.; Huang, M.; Yang, L.; Wang, G.; Guan, X. Facial Design and Synthesis of CoS_x/Ni-Co LDH Nanocages with Rhombic Dodecahedral Structure for High-Performance Asymmetric Supercapacitors. *Chem. Eng. J.* **2019**, *372*, 151–162. [CrossRef]
2. Mao, Y.; Xie, J.; Liu, H.; Hu, W. Hierarchical Core/Shell Ag@$Ni(OH)_2$@PPy Nanowire Electrode for Ultrahigh Energy Density Asymmetric Supercapacitor. *Chem. Eng. J.* **2021**, *405*, 126984. [CrossRef]
3. Kumar, J.; Jung, H.J.; Neiber, R.R.; Soomro, R.A.; Kwon, Y.J.; Hassan, N.U.; Shon, M.; Lee, J.H.; Baek, K.; Cho, K.Y. Recent Advances in Oxygen Deficient Metal Oxides: Opportunities as Supercapacitor Electrodes. *Int. J. Energy Res.* **2022**, *46*, 7055–7081. [CrossRef]
4. Gonçalves, J.M.; Silva, M.N.T.; Naik, K.K.; Martins, P.R.; Rocha, D.P.; Nossol, E.; Munoz, R.A.A.; Angnes, L.; Rout, C.S. Multifunctional Spinel $MnCo_2O_4$ Based Materials for Energy Storage and Conversion: A Review on Emerging Trends, Recent Developments and Future Perspectives. *J. Mater. Chem. A* **2021**, *9*, 3095–3124. [CrossRef]
5. Chen, H.; Du, X.; Liu, X.; Wu, R.; Li, Y.; Xu, C. Facile Growth of Nickel Foam-Supported $MnCo_2O_4$ Porous Nanowires as Binder-Free Electrodes for High-Performance Hybrid Supercapacitors. *J. Energy Storage* **2022**, *50*, 104297. [CrossRef]
6. Redekar, R.S.; Avatare, A.T.; Chouhan, J.L.; Patil, K.V.; Pawar, O.Y.; Patil, S.L.; Bhoite, A.A.; Patil, V.L.; Patil, P.S.; Tarwal, N.L. Review on Recent Advancements in Chemically Synthesized Manganese Cobalt Oxide ($MnCo_2O_4$) and Its Composites for Energy Storage Application. *Chem. Eng. J.* **2022**, *450*, 137425. [CrossRef]
7. Tang, P.; Gao, P.; Cui, X.; Chen, Z.; Fu, Q.; Wang, Z.; Mo, Y.; Liu, H.; Xu, C.; Liu, J.; et al. Covalency Competition Induced Active Octahedral Sites in Spinel Cobaltites for Enhanced Pseudocapacitive Charge Storage. *Adv. Energy Mater.* **2022**, *12*, 2102053. [CrossRef]
8. Zhang, J.; Yuan, X.; Si, M.; Jiang, L.; Yu, H. Core/Shell Structured Cadmium Sulfide Nanocomposites for Solar Energy Utilization. *Adv. Colloid Interface Sci.* **2020**, *282*, 102209. [CrossRef]
9. Liu, S.; Li, A.; Yang, C.; Ouyang, F.; Zhou, J.; Liu, X. MnO_2/Mn_2O_3 with Self-Triggered Oxygen-Defects for Superior Pseudoca-pacitive Energy Storage. *Appl. Surf. Sci.* **2022**, *571*, 151306. [CrossRef]
10. Xiong, S.; Lin, M.; Wang, L.; Liu, S.; Weng, S.; Jiang, S.; Xu, Y.; Jiao, Y.; Chen, J. Defects-Type Three-Dimensional Co_3O_4 Nanomaterials for Energy Conversion and Low Temperature Energy Storage. *Appl. Surf. Sci.* **2021**, *546*, 149064. [CrossRef]
11. Zhao, Y.; Hu, L.; Zhao, S.; Wu, L. Preparation of $MnCo_2O_4$@$Ni(OH)_2$ Core-Shell Flowers for Asymmetric Supercapacitor Materials with Ultrahigh Specific Capacitance. *Adv. Funct. Mater.* **2016**, *26*, 4085–4093. [CrossRef]
12. Li, X.; Wu, H.; Guan, C.; Elshahawy, A.M.; Dong, Y.; Pennycook, S.J.; Wang, J. (Ni,Co)Se_2/NiCo-LDH Core/Shell Structural Electrode with the Cactus-Like (Ni,Co)Se_2 Core for Asymmetric Supercapacitors. *Small* **2018**, *15*, 1803895. [CrossRef] [PubMed]
13. Li, K.; Zhao, B.; Bai, J.; Ma, H.; Fang, Z.; Zhu, X.; Sun, Y. A High-Energy-Density Hybrid Supercapacitor with P-$Ni(OH)_2$@$Co(OH)_2$ Core–Shell Heterostructure and Fe_2O_3 Nanoneedle Arrays as Advanced Integrated Electrodes. *Small* **2020**, *16*, 2001974. [CrossRef]
14. Sari, F.N.I.; Lin, K.-C.; Ting, J.-M. $Mn(OH)_2$-Containing $Co(OH)_2$/$Ni(OH)_2$ Core-Shelled Structure for Ultrahigh Energy Density Asymmetric Supercapacitor. *Appl. Surf. Sci.* **2022**, *576*, 151805. [CrossRef]
15. Man, P.; Zhang, Q.; Zhou, Z.; Chen, M.; Yang, J.; Wang, Z.; Wang, Z.; He, B.; Li, Q.; Gong, W.; et al. Engineering MoS_2 Nanosheets on Spindle-Like A-Fe_2O_3 as High-Performance Core–Shell Pseudocapacitive Anodes for Fiber-Shaped Aqueous Lithium-Ion Capacitors. *Adv. Funct. Mater.* **2020**, *30*, 2003967. [CrossRef]
16. Naveenkumar, P.; Maniyazagan, M.; Yesuraj, J.; Yang, H.-W.; Kang, N.; Kim, K.; Kalaignan, G.P.; Kang, W.S.; Kim, S.-J. Electrodeposited MnS@$Ni(OH)_2$ Core-Shell Hybrids as an Efficient Electrode Materials for Symmetric Supercapacitor Applications. *Electrochim. Acta* **2022**, *412*, 140138. [CrossRef]
17. Wang, G.; Yan, Z.; Ding, Y.; Xu, Z.; Li, Z. Hierarchical Core-Shell Nickel Hydroxide@nitrogen-Doped Hollow Carbon Spheres Composite for High-Performance Hybrid Supercapacitor. *J. Colloid Interface Sci.* **2022**, *628*, 286–296. [CrossRef]

18. Zong, Q.; Yang, H.; Wang, Q.; Zhang, Q.; Zhu, Y.; Wang, H.; Shen, Q. Three-Dimensional Coral-like NiCoP@C@Ni(OH)$_2$ Core-Shell Nanoarrays as Battery-Type Electrodes to Enhance Cycle Stability and Energy Density for Hybrid Supercapacitors. *Chem. Eng. J.* **2019**, *361*, 1–11. [CrossRef]

19. Ameri, B.; Zardkhoshoui, A.M.; Hosseiny Davarani, S.S. Engineering of Hierarchical NiCoSe$_2$@NiMn-LDH Core-Shell Nanostructures as a High-Performance Positive Electrode Material for Hybrid Supercapacitors. *Sustain. Energy Fuels* **2020**, *4*, 5144–5155. [CrossRef]

20. Liang, H.; Lin, J.; Jia, H.; Chen, S.; Qi, J.; Cao, J.; Lin, T.; Fei, W.; Feng, J. Hierarchical NiCo-LDH/NiCoP@NiMn-LDH Hybrid Electrodes on Carbon Cloth for Excellent Supercapacitors. *J. Mater. Chem. A* **2018**, *6*, 15040–15046. [CrossRef]

21. Sun, L.; Zhang, Y.; Zhang, Y.; Si, H.; Qin, W.; Zhang, Y. Reduced Graphene Oxide Nanosheet Modified NiMn-LDH Nanoflake Arrays for High-Performance Supercapacitors. *Chem. Commun.* **2018**, *54*, 10172–10175. [CrossRef] [PubMed]

22. Liu, G.; Huang, C.; Yang, Z.; Su, J.; Zhang, W. Ultrathin NiMn-LDH Nanosheet Structured Electrocatalyst for Enhanced Electrocatalytic Urea Oxidation. *Appl. Catal. A Gen.* **2021**, *614*, 118049. [CrossRef]

23. Kamari Kaverlavani, S.; Moosavifard, S.E.; Bakouei, A. Self-Templated Synthesis of Uniform Nanoporous CuCo$_2$O$_4$ Double-Shelled Hollow Microspheres for High-Performance Asymmetric Supercapacitors. *Chem. Commun.* **2017**, *53*, 1052–1055. [CrossRef] [PubMed]

24. Wei, G.; Zhao, X.; Du, K.; Huang, Y.; An, C.; Qiu, S.; Liu, M.; Yao, S.; Wu, Y. Flexible Asymmetric Supercapacitors Made of 3D Porous Hierarchical CuCo$_2$O$_4$@CQDs and Fe$_2$O$_3$@CQDs with Enhanced Performance. *Electrochim. Acta* **2018**, *283*, 248–259. [CrossRef]

25. Lu, X.-F.; Wu, D.-J.; Li, R.-Z.; Li, Q.; Ye, S.-H.; Tong, Y.-X.; Li, G.-R. Hierarchical NiCo$_2$O$_4$ Nanosheets@hollow Microrod Arrays for High-Performance Asymmetric Supercapacitors. *J. Mater. Chem. A* **2014**, *2*, 4706–4713. [CrossRef]

26. Wang, J.-G.; Jin, D.; Zhou, R.; Shen, C.; Xie, K.; Wei, B. One-Step Synthesis of NiCo$_2$S$_4$ Ultrathin Nanosheets on Conductive Substrates as Advanced Electrodes for High-Efficient Energy Storage. *J. Power Source* **2016**, *306*, 100–106. [CrossRef]

27. Felhi, H.; Smari, M.; Bajorek, A.; Nouri, K.; Dhahri, E.; Bessais, L. Controllable Synthesis, XPS Investigation and Magnetic Property of Multiferroic BiMn$_2$O$_5$ System: The Role of Neodyme Doping. *Prog. Nat. Sci. Mater. Int.* **2019**, *29*, 198–209. [CrossRef]

28. Ding, R.; Gao, H.; Zhang, M.; Zhang, J.; Zhang, X. Controllable Synthesis of Ni$_{3-x}$Co$_x$S$_4$ Nanotube Arrays with Different Aspect Ratios Grown on Carbon Cloth for High-Capacity Supercapacitors. *RSC Adv.* **2015**, *5*, 48631–48637. [CrossRef]

29. Poudel, M.B.; Kim, A.R.; Ramakrishan, S.; Logeshwaran, N.; Ramasamy, S.K.; Kim, H.J.; Yoo, D.J. Integrating the Essence of Metal Organic Framework-Derived ZnCoTe–N–C/MoS$_2$ Cathode and ZnCo-NPS-N-CNT as Anode for High-Energy Density Hybrid Supercapacitors. *Compos. Part B Eng.* **2022**, *247*, 110339. [CrossRef]

30. Bab u Poudel, M.; Chandra Lohani, P.; Kim, A.A. Synthesis of Silver Nanoparticles Decorated Tungsten Oxide Nanorods as High-Performance Supercapacitor Electrode. *Chem. Phys. Lett.* **2022**, *804*, 139884. [CrossRef]

31. Poudel, M.B.; Kim, H.J. Confinement of Zn-Mg-Al-Layered Double Hydroxide and α-Fe$_2$O$_3$ Nanorods on Hollow Porous Carbon Nanofibers: A Free-Standing Electrode for Solid-State Symmetric Supercapacitors. *Chem. Eng. J.* **2022**, *429*, 132345. [CrossRef]

32. Wu, N.; Zhao, W.; Zhou, B.; Wu, Y.; Hou, W.; Du, J.; Zhong, W. 3D nitrogen-doped Ti$_3$C$_2$T$_x$/rGO foam with marco-and microporous structures for enhance supercapacitive performance. *Electrochim. Acta* **2022**, *404*, 139752. [CrossRef]

33. Yang, Q.; Wang, Q.; Long, Y.; Wang, F.; Wu, L.; Pan, J.; Han, J.; Lei, Y.; Shi, W.; Song, S. In Situ Formation of Co$_9$S$_8$ Quantum Dots in MOF-Derived Ternary Metal Layered Double Hydroxide Nanoarrays for High-Performance Hybrid Supercapacitors. *Adv. Energy Mater.* **2020**, *10*, 1903193. [CrossRef]

34. Zhou, C.; Gao, T.; Wang, Y.; Liu, Q.; Huang, Z.; Liu, X.; Qing, M.; Xiao, D. Synthesis of P-Doped and NiCo-Hybridized Graphene-Based Fibers for Flexible Asymmetrical Solid-State Micro-Energy Storage Device. *Small* **2019**, *15*, 1803469. [CrossRef]